

Assessing thermal spike model of swift heavy ion-matter interaction via $\text{Pd}_{1-x}\text{Ni}_x/\text{Si}$ interface mixing

Paramita Patra,^{1,*} S. A. Khan,² M. Bala,³ D. K. Avasthi,⁴ and S. K. Srivastava^{5,†}

¹*Department of Physics, Indian Institute of Technology Kharagpur, Kharagpur - 721302, INDIA*

²*Inter-University Accelerator Centre, Aruna Asaf Ali Marg, New Delhi - 110067, INDIA*

³*Department of Physics and Astrophysics, University of Delhi, New Delhi - 110007, INDIA*

⁴*Amity Institute of Nanotechnology, Amity University, Sector 125, Noida - 201313, INDIA*

⁵*Department of Physics, Indian Institute of Technology Kharagpur, Kharagpur-721302, INDIA*

(Dated: August 17, 2021)

Thermal spike model (TSM) is presently a widely accepted mechanism of swift heavy ion (SHI) - matter interaction. It provides explanation to various SHI induced effects including mixing across interfaces. The model involves electron-phonon (e-p) coupling to predict the evolution of lattice temperature with time. SHI mixing is considered to be a result of diffusion in transient molten state thus achieved. In this work, we assess this conception primarily via tuning the e-p coupling strength by taking a series $\text{Pd}_{1-x}\text{Ni}_x$ of a completely solid soluble binary, and then observing 100 MeV Au ion induced mixing across $\text{Pd}_{1-x}\text{Ni}_x/\text{Si}$ interfaces. The extent of mixing has been parametrised by the irradiation induced change $\Delta\sigma^2$ in variances of Pd and Ni depth profiles derived from X-ray photoelectron spectroscopy. The x -dependence of $\Delta\sigma^2$ follows a curve that is concave upward with a prominent minimum. Theoretically, e-p coupling strength determined using density functional theory has been used to solve the equations appropriate to TSM, and then an equivalent quantity L^2 proportional to $\Delta\sigma^2$ has been calculated. L^2 , however, increases monotonically with x without any minimum, bringing out a convincing disparity between experiment and theory. Perhaps some mechanisms more than the TSM plus the transient molten state diffusion are operative, which can not be foreseen at this point of time.

PACS numbers: 61.80.Jh, 61.82.Bg, 68.35.Fx, 82.80.Pv

I. INTRODUCTION

While interacting with a solid, swift heavy ions (SHI's) are known to transfer a large amount of energy predominantly in the electronic subsystem of the solid.¹ At first hand, therefore, SHI's are not anticipated to cause any atomic displacements in the solid they interact with. However, irradiation of solids with SHI's has often been found to result in atomic displacements, which may cause, among various effects, mixing across interfaces in layered materials.²⁻⁴ There certainly has to be a mechanism by which the electronic energy, deposited by the SHI in the solid, gets transferred to the lattice atoms to cause such atomic displacements. At present, there are essentially two established models, viz., the Coulomb spike model (CSM) and the thermal spike model (TSM), to explain such atomic displacements.⁵⁻⁸ According to the CSM, a SHI, while passing through a solid material, ionizes the material in a cylindrical region around its path. The consequent strong collective electrostatic repulsion amongst the positive ions in the ionized zone leads to violent atomic displacements, resulting ultimately into a modified material in a cylindrical so-called ion track. This model, however, lacks applicability in metals, where the high mobility of conduction electrons leads to neutralization of charges much before the Coulomb explosion could occur. The TSM, on the other hand, assumes that the energy deposited initially in the electronic subsystem in a time scale of $10^{-15} - 10^{-14}$ s gets subsequently transferred to the lattice subsystem via electron-phonon

(e-p) coupling in $\sim 10^{-13} - 10^{-12}$ s. This results in a rapid rise in the lattice temperature (up to $\sim 10^4$ K) in a cylindrical zone of typically a few nm radius. In certain conditions a molten state is created along the ion track for a $\sim 10^{-12} - 10^{-11}$ s duration and is quenched rapidly (at a rate of $\sim 10^{14}$ K/s), freezing the molten modified state of the cylindrical zone. The modified frozen cylindrical zone thus formed is conventionally known as a latent track. If such melting happens across an interface between two materials, the atoms on the two sides inter-diffuse while in the molten state, giving rise to mixing across the interface.⁸ The mechanism suggests that the TSM must be applicable in metals, semiconductors and insulators alike. The model has acquired a wide acceptance in course of time.

The TSM is mathematically described by the following two coupled partial differential equations, which are basically the constituents of the so-called two temperature model (TTM) and govern the diffusion of the energy brought in by the ion into the electronic and lattice subsystems:^{5,9}

$$C_e(T_e)\frac{\partial T_e}{\partial t} = \nabla \cdot (K_e(T_e)\nabla T_e) - (T_e - T_l)G(T_e) + A_e(r, t)$$

and

$$C_l(T_l)\frac{\partial T_l}{\partial t} = \nabla \cdot (K_l(T_l)\nabla T_l) + (T_e - T_l)G(T_e). \quad (1)$$

Here, C_e , C_l and K_e , K_l stand for specific heats and thermal conductivities of the electronic and lattice subsystems, and T_e and T_l are the electronic and lattice temperatures, respectively. $G(T_e)$ is the electronic temperature dependent e-p coupling strength, and $A_e(r, t)$ is

the energy density per unit time supplied by the incident ions to the electronic system at time t and at radius r from the ion path in such a way that the integral $\int \int 2\pi r A_e(r, t) dr dt$ is equal to the electronic energy loss S_e , defined as the energy deposited by the ions in the electronic subsystem per unit length travelled in the solid.

A direct experimental proof of the validity of the TSM has hitherto not been possible because of the extremely short time scales involved. A number of ion fluence dependent SHI induced effects observed experimentally have been used to coarsely derive the latent track radii, which have been found comparable with those calculated roughly from the mathematical equations pertaining to the TSM.⁸ These provide a highly indirect and very crude indication of the occurrence of SHI induced processes as hypothesized in the TSM. In all these reports, the free electron theory of metals, which predicts a parabolic density of electron states (eDOS), has been used to determine the electronic part of the thermophysical parameters, viz. C_e , K_e and $G(T_e)$,^{5,10} to be used in the TTM equations. Accordingly, C_e is given by⁵

$$C_e(T_e) = \frac{\pi^2 g(\epsilon_F) k_B^2}{2\epsilon_F} T_e, \quad (2)$$

K_e is related with C_e via electronic thermal diffusivity $D_e(T_e)$ by a relation

$$K_e(T_e) = C_e(T_e) D_e(T_e), \quad (3)$$

and $G(T_e)$ is determined using

$$G_e(T_e) = \frac{\pi^4 [g(\epsilon_F) k_B v_s]^2}{18 K_e(T_e)}. \quad (4)$$

Here, $g(\epsilon_F)$ is the eDOS at the Fermi energy ϵ_F , and k_B is the Boltzmann constant. The phonon contribution to the e-p coupling strength appears in the form of the speed v_s of sound in the solid. However, a couple of reports on 120 MeV Au induced mixing in Si/M/Si (M = V, Fe, Co, Mn, Nb) layered structures^{11,12} suggested that the relatively more localized d -electrons, which bring in features to the eDOS over the parabolic background, also have influence on the efficiency of SHI mixing. This necessitates the consideration of exact electron density of states $g(\epsilon)$ as a function of energy ϵ , computable using *first-principles* density functional theory (DFT), to derive the thermophysical quantities required for the TTM. The following forms of C_e and $G(T_e)$, as reported by Lin *et al.*,¹³ would be more appropriate in this scenario:

$$C_e(T_e) = \int_{-\infty}^{\infty} g(\epsilon) \left[\frac{\partial f(\epsilon, T_e)}{\partial T_e} \right] \epsilon d\epsilon \quad (5)$$

and

$$G(T_e) = \frac{h k_B \lambda \langle \omega^2 \rangle}{2g(\epsilon_F)} \int_{-\infty}^{\infty} g^2(\epsilon) \left[- \frac{\partial f(\epsilon, T_e)}{\partial \epsilon} \right] d\epsilon, \quad (6)$$

where h is the Planck's constant and $f(\epsilon, T_e)$ is the Fermi-Dirac distribution function given by $f(\epsilon, T_e) = 1/[1 + \exp\{(\epsilon - \epsilon_F)/k_B T_e\}]$. The electron band mass enhancement factor λ ^{14,15} and the second moment $\langle \omega^2 \rangle$ of the phonon spectrum¹⁶ can be obtained from *ab initio* phonon bandstructure calculations. Lin *et al.*,¹³ this way, have calculated electron temperature dependent electronic specific heats and electron phonon coupling strengths for a number of noble and transition metals, and have reported a substantial difference between the free-electron and full eDOS values. In a recent work,¹⁷ we have shown how slight variations of $g(\epsilon)$ for different orientations of a thin Bi₂Te₃ slab result into different $C_e(T_e)$ and $G(T_e)$ curves.

If the TSM is valid, the use of equations (6) and (7), instead of (3) and (5), in the TTM equations ought to improve the predicting ability of the model for getting an outcome of a SHI-matter interaction experiment. To enact this, conducting a series of SHI-matter interaction experiments, e.g. SHI driven interface mixing across a number of thin film/substrate interfaces, with one kind of substrate and different kinds of thin films of differing C_e and G values, would be helpful. As far as the rest of TTM parameters, viz. K_e , C_l and K_l , are concerned, they could, to an appreciable extent, be predictable or obtainable from literature for each film. One possibility could be taking a series of M/Si interfaces with different metals M so that the eDOS and the resultant C_e and G values could be calculated for each M. However, the K_e , C_l and K_l values might be arbitrarily different for different M, a case which is obviously undesirable. An appropriate choice for M would be to take thin films A_{1-x}B_x of a complete solid-soluble binary metal system with $0 \leq x \leq 1$. For such a series, $g(\epsilon)$, C_e and G would be easily computable for each x . Furthermore, the K_e , C_l and K_l values will have a smooth (to the first approximation linear) variation with x .¹⁸ One such system is Pd_{1-x}Ni_x binary alloy system, which forms a complete solid solution throughout the whole composition range without any change of the crystal structure, as depicted by their equilibrium phase diagram.¹⁹

The present work aims at convincingly assessing the thermal spike model by (i) experimental determination of the x -variation of efficiency of SHI driven mixing of Pd and Ni in Si via 100 MeV Au irradiation of Pd_{1-x}Ni_x/Si system, (ii) computation of x -variation of C_e and G using DFT, and then use of the TTM equations to qualitatively estimate the expected x -variation of extent of mixing, and (iii) a comparison between the experimental and computational results. Any slight variation in the computationally predicted efficiency of mixing should be observable also in the experimental results if the TSM is indeed the mechanism of SHI matter interaction. However, neither Pd nor Ni is known to be mixed with Si by SHI's; Pd/Si or Ni/Si mixing has only been reported to be induced by low energy ions,^{20,21} where elastic collisions are responsible for the process. In the present work also, Pd/Si or Ni/Si mixing in the Pd_{1-x}Ni_x/Si system

has not been observed as an immediate effect of the irradiation; it is rather the Ar^+ ion sputtering process in the subsequent X-ray photoelectron spectroscopy (XPS) depth profiling that augments the effects of SHI's and leads to observable mixing. Since the sputtering conditions are the same for all the samples, any x -variation of extent of mixing should have indirectly been driven by the SHI irradiation. Such a combination of SHI irradiation and XPS depth profiling to enable one to observe SHI effects in the form of interface mixing has hitherto not been reported.

II. EXPERIMENTAL AND COMPUTATIONAL DETAILS

Prior to depositing the $\text{Pd}_{1-x}\text{Ni}_x$ ($x \neq 0, 1$) alloy thin films on Si substrates, the alloys were first prepared by Ar arc melting. Palladium wire of 99.9% purity and nickel foil of 99.994% purity were melted together to prepare the alloys. The alloyed ingots were flipped and remelted to improve the homogeneity. Subsequently, Pd and Ni metals, and two compositions $x = 0.40$ and 0.78 of $\text{Pd}_{1-x}\text{Ni}_x$ alloys were deposited onto pre-cleaned Si substrates by electron beam evaporation. The pressure during deposition was $\sim 1.7 \times 10^{-7}$ torr, and the deposition rate ranged from 0.1 to 0.3 \AA/s . The thicknesses of the four $\text{Pd}_{1-x}\text{Ni}_x$ ($x = 0, 0.40, 0.78$ and 1) films were in $25 - 40$ nm range, as determined from Rutherford backscattering spectra (RBS) and XPS depth profiles to be discussed in the following sections. For all the samples, $1 \text{ cm} \times 1 \text{ cm}$ pieces were taken out for irradiation by 100 MeV Au ions each at 1×10^{14} ions/cm² fluence using the 15 UD Pelletron accelerator at Inter University Accelerator Centre (IUAC), New Delhi. The electronic (S_e) and nuclear (S_n) energy losses of the ions in Pd are 34.10 keV/nm and 0.09 keV/nm , respectively, as calculated from the SRIM software.²² The two values for Ni are 32.40 keV/nm and 0.08 keV/nm , respectively. Thus, the electronic energy losses are dominant and hence the condition is relevant to the present study. The pristine and irradiated samples were characterized by X-ray diffraction (XRD), RBS, and XPS depth profiling. XRD patterns for all the samples were recorded using $\text{Cu K}\alpha$ radiation from a Philips X'Pert MRD X-ray diffractometer in the 2θ range of $20^\circ - 80^\circ$. The RBS measurements were performed using 2 MeV He^+ ions from the PARAS facility of IUAC, and were undertaken to determine the thickness and composition of the samples. The XPS depth profiles were carried out using a PHI 5000 Versaprobe II machine under DST-FIST scheme.

The DFT computations were performed using the code Wien2K,²³ which is based on a full-potential linearized augmented plane wave (FLAPW) method. Pd, Ni and all the solid solutions crystallize in an fcc lattice with space group $\text{Fm}\bar{3}\text{m}$.¹⁹ $x = 0, 0.25, 0.5, 0.75$ and 1 were taken for the computations. Pd and Ni ($x = 0, 1$) structures were first constructed by taking literature values of the

respective lattice constants, and then by optimizing the volume, so that the equilibrium lattice constants correspond to the respective minimum energy configurations. Birch-Murnaghan equation of state^{24,25} was used to fit the energy versus volume curves for the optimizations. The crystal structure for $x = 0.25$ (0.75) was generated by constructing a $1 \times 1 \times 2$ supercell of Pd (Ni) and then replacing one of the four site-split Pd (Ni) atoms with Ni (Pd). For the case of $x = 0.5$, 2 of the four site-split Pd atoms in a $1 \times 1 \times 1$ supercell were replaced with Ni. All these structures were separately volume-optimized by the same procedure as stated above. For the $x \neq 0$ structures, the atomic coordinates were further relaxed to limit the atomic forces to less than 1 mRy/au . The exchange-correlation functionals adopted for the calculations were taken according to the generalized gradient approximation (GGA) as introduced by Perdew, Burke and Ernzerhof.²⁶ The energy of separation between core and valence states was taken as -0.6 Ry . In the FLAPW method, the potential in a Muffin-tin radius R_{MT} around each atom is taken as atomic-like, and atomic spherical wavefunctions are used as basis functions for the basis set,²⁷ while in the interstitials, the potential is smooth and plane waves constitute the basis functions. The R_{MT} value for both Pd and Ni was taken as 2.5 a.u. In all the calculations, the wavevectors for plane waves were kept limited to a maximum value k_{max} such that $k_{max}R_{MT} = 7.0$. The maximum multipolarity l_{max} for the spherical wavefunctions was set at 10 . Further, the Fourier expansion of the charge density was limited to $G_{max} = 12$. The Brillouin zone was sampled using a k -mesh with 72 irreducible k -points.

From the eDOS's as computed from the DFT method described above, $C_e(T_e)$ and $G(T_e)$ were calculated using equations (6) and (7) for each composition. For the latter, in addition, $\lambda\langle\omega^2\rangle$ values were taken from literature for pure Pd and Ni, which were then linearly interpolated to get the values for intermediate compositions. For the TTM calculations in the next step, $C_e(T_e)$ and $G(T_e)$ values for temperature ranges taken usually in a TSM code²⁸ were sampled out from the derived $C_e(T_e)$ and $G(T_e)$ curves, and used as inputs to the code. The rest of the parameters, viz. K_e , C_l and K_l were interpolated between Pd and Ni values in the same manner as $\lambda\langle\omega^2\rangle$ values were derived for calculating $G(T_e)$.

III. RESULTS AND DISCUSSION

A. XRD

X-ray diffraction patterns of all the samples before and after irradiation are shown in Figs. 1 (a) - (d). Peaks corresponding to Pd, Ni and Si elemental solids have been identified from the corresponding Joint Committee on Powder Diffraction Standards (JCPDS) data. The peaks of the compounds, on the other hand, have been identified by a comparison with the powder diffraction pat-

terns simulated using PowderCell²⁹ and by taking the crystal parameters for NiSi, Ni₃Si₂ and Ni₂Si from Ref. [30] and for PdSi³¹ and Pd₂Si³² from SpringerMaterials online database. A look at the XRD patterns of the pristine samples indicates the presence of a combination of elemental and compound phases mentioned above. The elemental peaks are as expected, while the compounds (silicides) must have been formed during the film deposition. Silicide formation while depositing thin metal films on Si is not uncommon.³³

The common effect of irradiation of all the samples has been either a complete removal or a significant suppression or broadening of almost all but the substrate peaks. This must be due to SHI irradiation induced defect creation and amorphization of the films. Such irradiation induced effects are also not uncommon.³⁴ The takeaway message from the XRD patterns is that (i) the samples contain thin films of a combination of elemental and silicide phases, and (ii) SHI irradiation does produce structural modifications in the samples. Any further interpretation of the XRD patterns would perhaps become an over-interpretation.

B. RBS

RBS spectra of all the pristine and irradiated samples were recorded to determine the compositions and thicknesses of the thin films, and also to examine whether there is any interface mixing occurring as a consequence of the irradiation alone. The spectra and their fits using the code SIMNRA³⁵ are shown in Figs. 2(a) - (d). According to the fits, the samples have configurations Pd (19.2 nm)/Si, Pd_{0.60}Ni_{0.40} (28.8 nm)/Si, Pd_{0.22}Ni_{0.78} (18.8 nm)/Si and Ni (23.0 nm)/Si. The spectra were fitted using a resolution in the range of 20 - 24 keV, which is equivalent to ~ 12 nm. An insignificant but noticeable decrease in Pd and Ni peak intensities after irradiation for all the samples indicates that Pd/Si and Ni/Si interface mixing might have taken place as a consequence of irradiation. However, the mixing thicknesses must be too small compared to the resolution (~ 12 nm) to show up in the spectra to any significant extent. In order to investigate whether there is indeed a SHI induced mixing, XPS depth profiles, which could provide a much better spatial resolution, have been performed on all the pristine and irradiated samples. The results are discussed in the following section.

C. XPS depth profile

All the samples have been analyzed using depth profiling XPS paired with 1 keV Ar⁺ ion sputtering to collect Pd3d, Ni2p and Si2p high-resolution spectra. A large number of sputtering cycles were used for the study so that the film/substrate interface is reached in about 35 - 40 cycles. A comparison of these many number of sput-

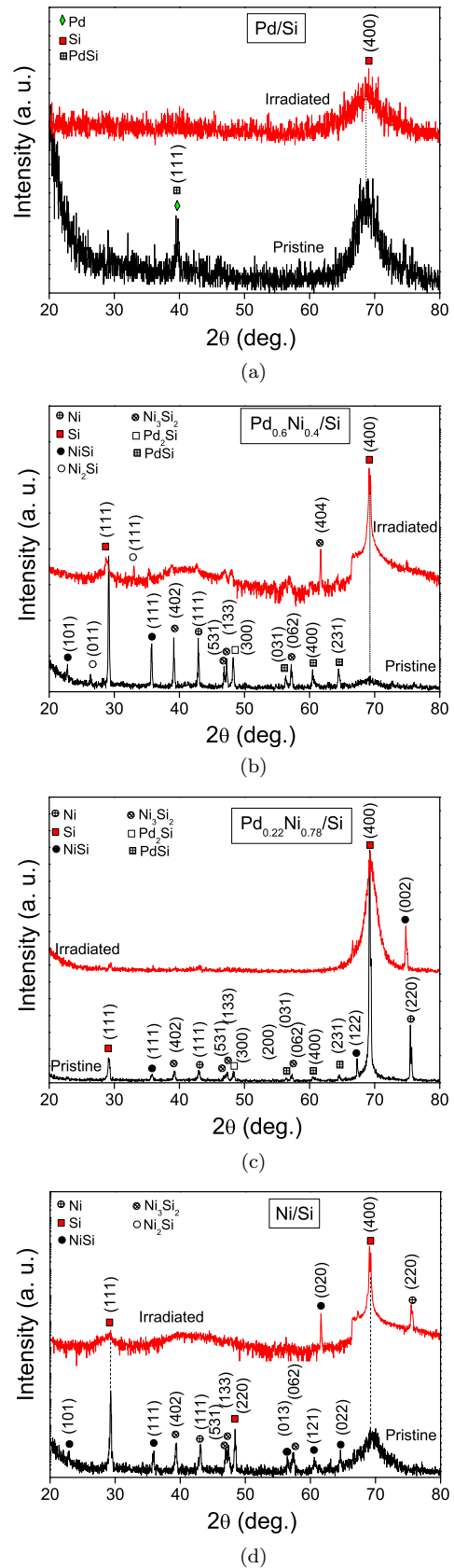


FIG. 1: XRD spectra of (a) Pd/Si (b) Pd_{0.22}Ni_{0.78}/Si (c) Pd_{0.60}Ni_{0.40}/Si and (d) Ni/Si. The steps at $\sim 67^\circ$ in (b) and (d) are experimental artefacts, and do not affect the interpretations made.

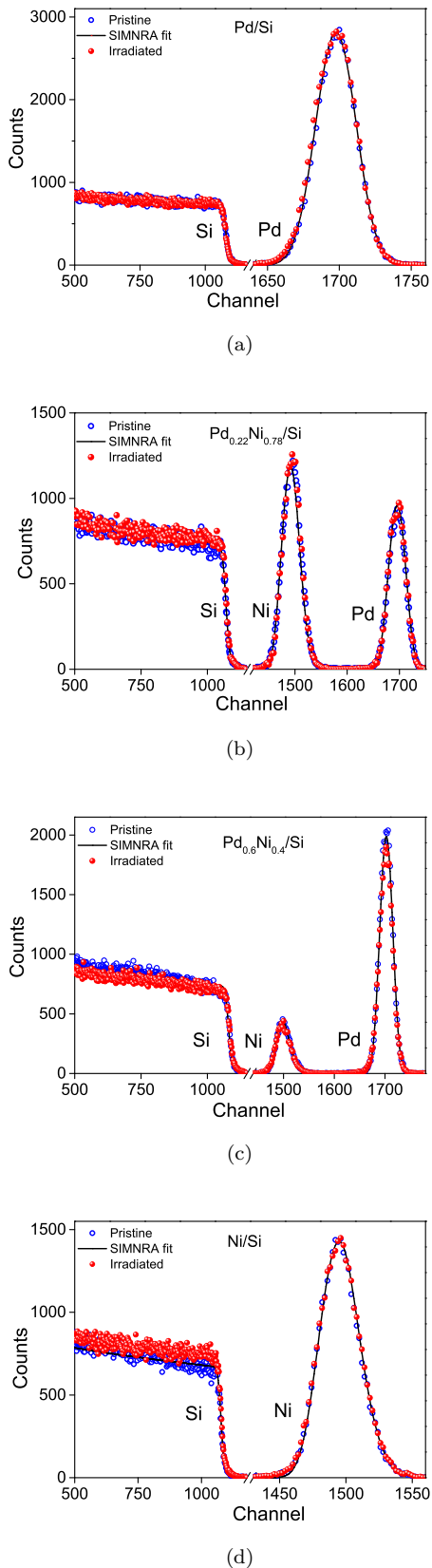


FIG. 2: RBS spectra of (a) Pd/Si (b) Pd_{0.22}Ni_{0.78}/Si (c) Pd_{0.60}Ni_{0.40}/Si and (d) Ni/Si

ter cycles (to reach the interface) with the depth of the interface (i.e., the film thickness) indicates that the XPS spectra have been recorded at the interval of 0.5 - 0.6 nm. This is likely to provide a (minimum) depth resolution of 0.5 - 0.6 nm for elemental depth profiling, a spatial depth resolution at least an order of magnitude better than the RBS depth resolution mentioned above, and hence to enable us to observe any small amount of SHI induced interdiffusion (or intermixing) of Pd or Ni into Si and vice-versa. It should be noted here, though, that the Ar⁺ ion sputtering process itself can induce an additional interface mixing.³⁶ However, since its effects are similar for all the samples, any x -variation of observed mixing can be taken essentially as the SHI irradiation effect, which is augmented further by the sputtering induced mixing equally. We will be comparing the experimentally observed x -variation of mixing with the x -variation of an equivalent quantity estimated using DFT and TTM computations.

Figure 3 shows the high-resolution XPS spectra in Pd 3d_{5/2}, Ni 2p_{3/2} and Si 2p_{3/2} regions of the pristine and irradiated Pd_{0.60}Ni_{0.40}/Si samples for different sputter cycles. This composition has been taken as a representative for all the samples. For both the pristine and irradiated samples, both the Pd and Ni XPS peaks (i) diminish gradually and (ii) shift to higher binding energies (BE's), while approaching the interface. The Si peak also has a gradual rise from the interface, with a less pronounced shift. The gradual changes in the peak heights are indicative of interdiffusion or intermixing of Pd and Ni in Si even in the pristine sample. The intermixed interface seems to broaden on irradiation, as can be seen from the apparently deeper interpenetrations of the peaks in the interfacial region. These observations can be made more quantitative by plotting the XPS peak position at maximum intensity (PPMI) versus sputter cycle (SC).

Figure 4 displays the PPMI versus SC plots in Pd 3d_{5/2}, Ni 2p_{3/2} and Si 2p_{3/2} regions of the pristine and irradiated Pd_{0.60}Ni_{0.40}/Si samples. The symbol sizes are proportional to the corresponding normalized intensities. It is to be noted that the PPMI's as plotted in the figure are not true single peak positions, as each of the Pd 3d_{5/2}, Ni 2p_{3/2} and Si 2p_{3/2} peaks may consist of more than one sub-peaks signifying different elemental or compound phases. A deconvolution of these peaks, which will be shown in the following, would identify the phases present. Coming back to the PPMI versus SC plots, the PPMI for pristine Ni shifts continuously from 852.25 eV at SC 32 to 853.75 at SC 47 with concomitantly diminishing intensity. The trend continues beyond the 47th cycle with the PPMI saturating at 854 eV. The concomitant PPMI shift and intensity reduction is indicative of an increase in the number of Si atoms surrounding a Ni atom, and hence suggests the occurrence of diffusion of Ni into Si substrate.^{37,38} The PPMI profile with SC, thus, can be considered to represent the reverse Ni concentration profile with depth (depth profile). The middle (around SC 40) of the interfacial interdiffused region (SC 32 to

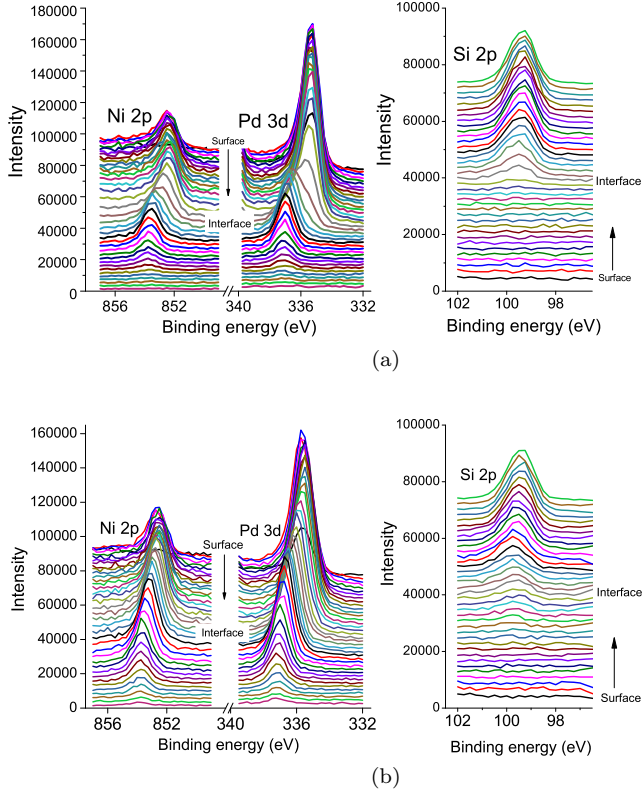


FIG. 3: High-resolution XPS spectra in Pd $3d_{5/2}$, Ni $2p_{3/2}$ and Si $2p_{3/2}$ regions of Pd_{0.60}Ni_{0.40}/Si pristine (a) and irradiated (b) samples for different sputter cycles. The curves corresponding to the surface and interface are indicated. For clarity, the spectra of alternate cycles only have been plotted.

SC 47) can be considered as the true film substrate interface. Equating SC 40 to 28.8 nm as obtained from the RBS results, the interdiffusion region extends from about 23.0 nm to about 33.8 nm, i.e. in a span of about 10.8 nm. This can be considered as the standard deviation σ of the interfacial position, or in other words the interface width, for the present depth profile. This Ni-Si interdiffusion has taken place during the deposition itself, as has also been argued in the XRD subsection above. The effect of 100 MeV Au irradiation, augmented by the Ar⁺ ion sputtering during the depth profiling, has been to broaden the PPMI profile such that the PPMI shifts from 852.25 eV at SC 30 to 853.75 at SC around 55, once again with continuously diminishing intensity. The standard deviation after irradiation, thus, becomes 25 sputter cycles, which is equivalent to 18.0 nm. As the irradiation itself has been shown to cause modifications in the sample as revealed from the XRD patterns, the irradiation can be considered as the primary source of the relative interface broadening or the enhanced interdiffusion. The enhanced interdiffusion, in turn, can be considered to represent the 100 MeV Au (i. e., SHI) in-

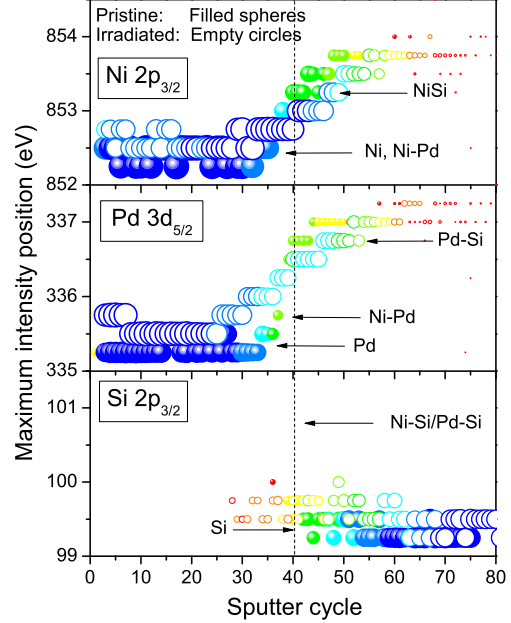


FIG. 4: Binding energy positions of maximum intensity versus sputter cycle in Pd $3d_{5/2}$, Ni $2p_{3/2}$ and Si $2p_{3/2}$ regions of Pd_{0.60}Ni_{0.40}/Si pristine and irradiated samples. The symbol sizes and colours signify the intensity of the maximum for a particular sputter cycle normalized with respect to the maximum intensity which is maximum of all for each region and sample condition (pristine or irradiated). Tentative elements or compound phases corresponding to different peak positions are also shown for a guidance. The apparent film substrate interface is marked with a dashed line.

duced mixing. The PPMI profile of Pd also follows the same pattern, the only difference being that the σ value changes from 11 cycles (9.8 nm) for the pristine sample to 26 cycles (19.4 nm) after irradiation. In the case of Si, the intensity starts decreasing from about the same depth till which Pd and Ni interdiffuse for both pristine and irradiated samples separately. Further, the presence of Si extends, with diminishing intensity, into the film till the depth from where Pd and Ni had started depleting. Although the Si peak shifts are small, and hence likening it to a concentration versus depth profile would not be very convincing, its simultaneous presence with Pd and Ni corroborates the conjecture of interdiffusion of Pd and Ni in Si, which increases as a result of irradiation. The interfacial broadening can be better quantified by determining the atomic fractions of the elements using the areas under the peaks and the elemental sensitivity factors, and then plotting these against the depth, scaled appropriately from the sputter cycle. These depth profiles for all the pristine and irradiated samples will be shown and discussed later.

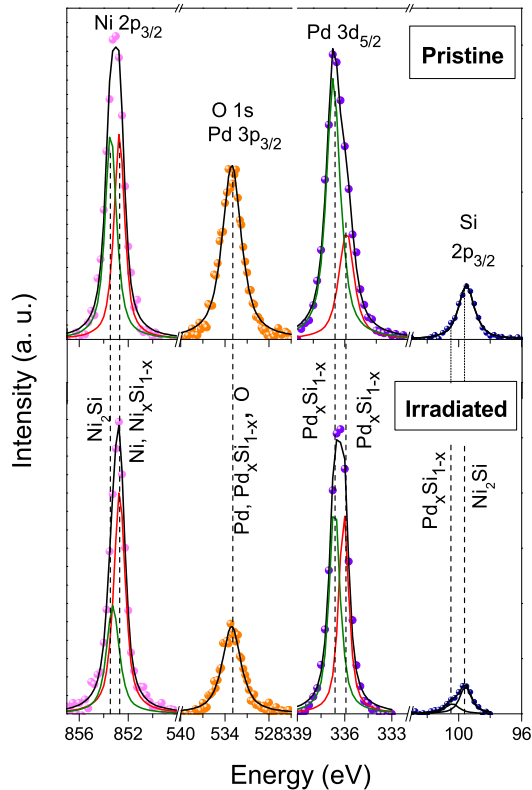


FIG. 5: The background corrected high-resolution XPS spectra in Si $2p_{3/2}$, Pd $3d_{5/2}$, O $1s$ and Ni $2p_{3/2}$ regions (shown in top panel) and their fits for the Pd_{0.60}Ni_{0.40}/Si pristine and irradiated samples. O $1s$ and Pd $3p_{3/2}$ spectra overlap⁴⁴. Tentative assignments of different peak positions (bottom panel) are also shown.

It would be worthwhile in the meantime to examine the XPS spectra of these samples at the interface (SC 40) to see the interfacial phases present before and after irradiation. The background corrected high-resolution XPS spectra in Si $2p_{3/2}$, Pd $3d_{5/2}$, O $1s$ and Ni $2p_{3/2}$ regions and their fits for the Pd_{0.60}Ni_{0.40}/Si pristine and irradiated samples are shown in Fig. 5. Tentative assignments of different peak positions to pure³⁹ Pd and Ni and their silicides with random compositions (e.g., Pd_{*x*}Si_{1-*x*}⁴⁰⁻⁴²) or in compound form, like Ni₂Si^{42,43}, and to adsorbed oxygen,⁴⁴ are also shown. In brief, both the pristine and irradiated Pd_{0.60}Ni_{0.40}/Si samples contain elemental and silicide phases of Pd and Ni at the interface with slightly different amounts before and after irradiation. The irradiated sample has an additional Pd_{*x*}Si_{1-*x*} peak. These conjectures are in agreement with the XRD observations, as discussed earlier.

Moving on to the depth profiles, these are shown in Figs. 6 (a) - (d) as variations of atomic fractions (concentrations, *m*) of Pd, Ni and Si as a function of depth

z for the four studied samples. Here, the SC has been converted to depth with the help of RBS analyses as discussed above. The depth profiles have been obtained using the quantification scheme provided in the MultiPak Data Reduction Software available with the PHI 5000 Versaprobe II XPS instrument used for measuring XPS spectra. Absence of sharp interfaces even in the pristine samples, as can be seen from figures, suggests that there is already an interdiffusion in the pristine samples, in line with the earlier arguments. This interdiffusion might have taken place during the film deposition, and may have further been augmented by Ar⁺ ion sputtering during the depth profiling.

The Pd and Ni depth profiles have been roughly fitted with error function, and the fits are shown overlapping with the data. The squared interface width, or variance, σ^2 has then been calculated using⁴⁵

$$\sigma^2 = \frac{\int_0^\infty z^2 m'(z) dz}{\int_0^\infty m'(z) dz}, \quad (7)$$

where $m'(z)$ is the gradient of the fitted interface profile. The change $\Delta\sigma^2$ in variance on irradiation for a particular depth profile is then given by the difference in the variances after and before irradiation. The value 265 ± 30 nm of $\Delta\sigma^2$ for Ni in Si for the case of $x = 0.40$ can be compared with $(18 \text{ nm})^2 - (10.8 \text{ nm})^2 \sim 208 \text{ nm}^2$, as obtained using the PPMI versus SC plots discussed above. These values are fairly close to each other.

Figure 7 shows the variation of $\Delta\sigma^2$, for Pd and Ni interdiffusion in Si, with Ni concentration x . It is noteworthy that $\Delta\sigma^2(x)$ is neither flat nor monotonic; it rather has a pronounced minimum. The crudest approximation to this variation would be a curve which is concave upward and has a rather deep minimum. In the following sections, we would attempt to examine whether such a variation can be simulated computationally based on the concepts of TSM and DFT.

The strategy for doing the calculations is as follows: (i) Assume the validity of TSM. (ii) Use the TTM equations (1) and (2) to see the evolution of Pd_{1-*x*}Ni_{*x*} lattice temperature, at various radial distances from the ion track, with time. At this stage, use DFT to compute C_e and G appropriate to be taken as inputs to the TTM equations (6) and (7). For this, construct Pd_{1-*x*}Ni_{*x*} crystal structures of various compositions close to the experimental ones and calculate electron densities of states $g(\epsilon)$. Limit the TSM calculations to bulk Pd_{1-*x*}Ni_{*x*}, as Si is common substrate to all the samples and hence its influence is likely to have no x dependence. (iii) See if the Pd_{1-*x*}Ni_{*x*} lattice melts. Otherwise, record the x variation of an average lattice temperature T_{av} achievable in the lattice at a fixed r , and then derive a quantity which could be correlated with $\Delta\sigma^2$. (iv) See whether the variations of this quantity with x follows any concave upward trend.

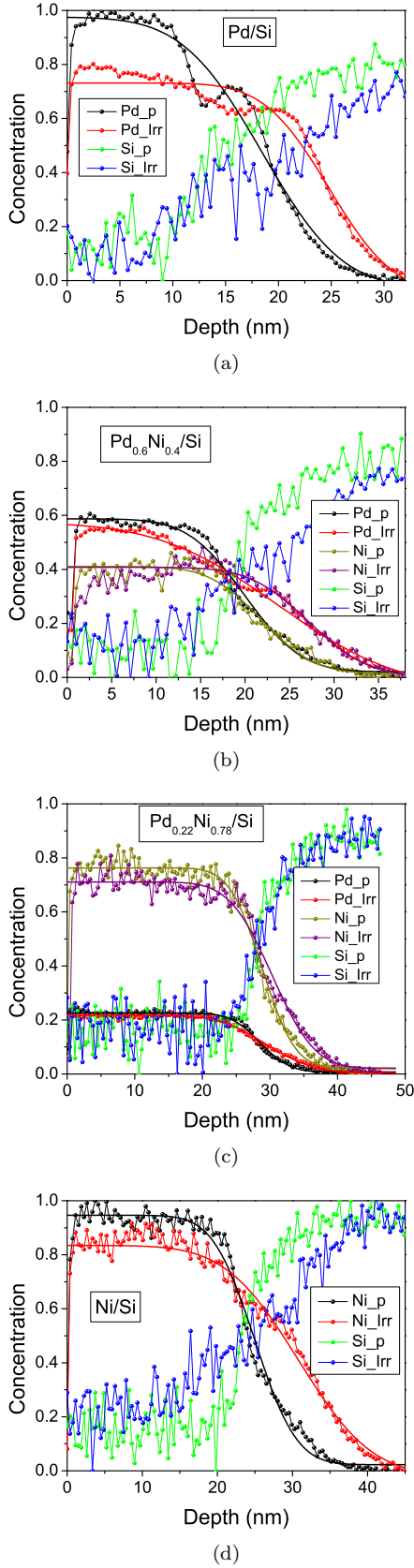


FIG. 6: XPS depth profile of (a) Pd/Si (b) Pd_{0.22}Ni_{0.78}/Si (c) Pd_{0.60}Ni_{0.40}/Si and (d) Ni/Si. Overlapped with Pd and Ni profiles are their error function fits.

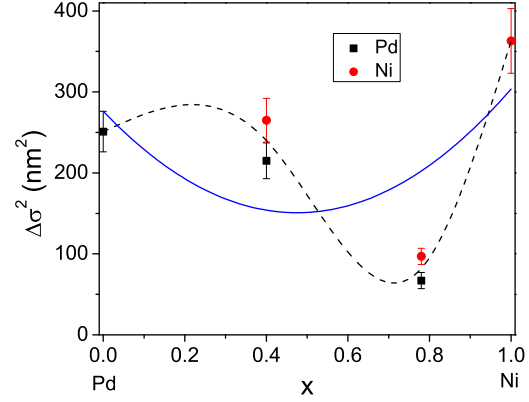


FIG. 7: Variation of $\Delta\sigma^2$ with x for Pd and Ni interdiffusion in Si. The dotted line is a guide to the eyes. The concave upward curve shown as continuous line is the crudest approximation for this variation.

D. $g(\epsilon)$, C_e and G

The first step for the calculations is to compute $g(\epsilon)$ using DFT. Figure 8 displays the $g(\epsilon)$ curves for Pd_{1-x}Ni_x ($x = 0, 0.25, 0.5, 0.75, 1$) alloys. Without interpreting the densities of states, which themselves are rich of information like $g(\epsilon_F)$, the underlying orbital hybridizations, etc. and their variation with x , which in turn may shed light on the electronic and magnetic properties of the Pd_{1-x}Ni_x alloys,⁴⁶ we move over to directly using them as an input to the TTM equations. We restrict the refinements of the parameters used in the TTM equations only to the electronic part, which is accessible through DFT. For the rest of the parameters, like even the phonon part $\lambda\langle\omega^2\rangle$ in Eq. (7), we take, as the first approximation, the terminal ($x = 0, 1$) values from literature, and linearly interpolate these values for the intermediate compositions. The $\lambda\langle\omega^2\rangle$ values taken for $x = 0$ and 1 are 41 meV² and 63 meV², respectively^{5,14}. Figure 9 (a) displays the variations of C_e and G , respectively, with T_e for the computed Ni compositions. Instead of investigating how these parameters vary with T_e , finding out how they vary with x for representative electronic temperatures would be more relevant. $C_e(x)$ at 5000 K and $G(x)$ at 300 K, the two temperatures being representative ones to be used as inputs in the TSM calculations, are shown in Fig. 9 (b). Thus comes the first milestone of comparison with the experiment: qualitatively, the two parameters increase monotonically with x almost together, do have a shallow concave upward nature, but do not possess a minimum. We now move forward to performing the TSM calculations.

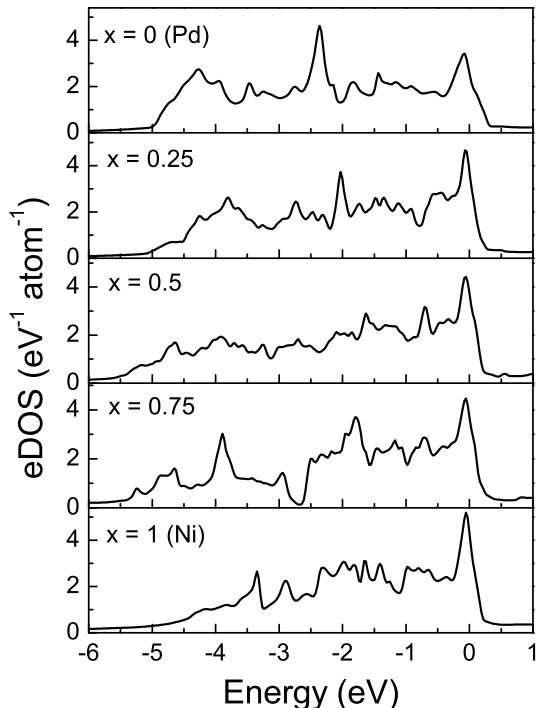


FIG. 8: The electronic densities of states of the $\text{Pd}_{1-x}\text{Ni}_x$ alloy system.

E. TSM calculations

Table I enlists the additional input parameters that have been used in the TTM equations (1) and (2) in order to proceed with the TSM calculations. Figures 10 (a) and (b) show the evolution of lattice temperature with time at different radial distances from ion path for the terminal ($x = 0$ and 1, respectively) systems, taken as representative ones. As can be observed, the lattice does not reach its melting temperature¹⁹ in either case. This is true for all the compositions, not all shown here though. Thus, occurrence of molten state diffusion, the requirement for SHI induced interface mixing according to the TSM, is out of question in the present case. If the TSM is valid, any possible interdiffusion must have taken place in the solid state itself while the lattice was hot, and then would have got enhanced by the sputtering. To investigate this aspect, we analyse the TSM results in the following way.

Since we are interested in finding out only the x variations of the derived quantities, we can look at the evolution of lattice temperature with time, at a common radial distance, say 1 nm, for all x . This is plotted in Fig. 10 (c). As far as diffusion (of Pd and Ni in Si separately) is concerned, we need to derive an appropriate average temperature T_{av} at which the diffusion can be considered to have taken place, and the average duration Δt for the diffusion. A suitable choice for selecting the two quantities for a particular x would be to take FWHM of the

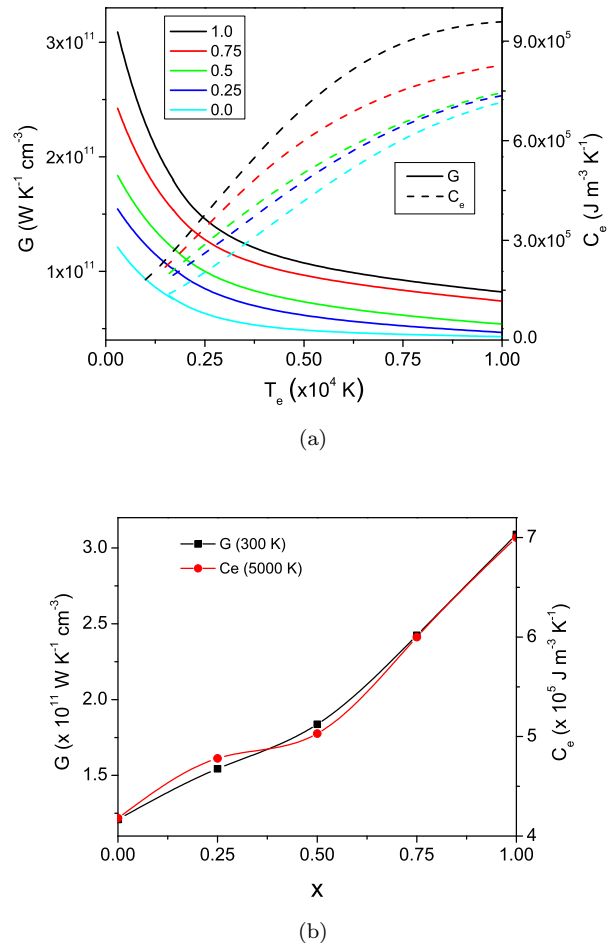


FIG. 9: Variations of (a) specific heat (dotted curves) and e-p coupling strength (continuous lines) with electron temperature, and (b) of both with Ni composition. The lines in (b) are a guide to the eyes.

TABLE I: Lattice specific heat (C_l), electronic thermal conductivity (K_e), lattice thermal conductivity (K_l) and electronic energy loss (S_e), used as inputs to the TSM calculations.

Parameter	unit	$x = 0$	$x = 1$	Ref.
C_l	J/g-K	0.12 - 0.30	0.27 - 0.60	[5]
K_e	W/cm-K	0.05	0.05	[5]
K_l	W/cm-K	2.33 - 0.78	11.33 - 0.50	[5]
S_e	keV/Å	3.41	3.24	[28]

corresponding T_l versus t curve at 1 nm radial distance. This sets T_{av} at the temperature where the half maximum of the curve occurs, while Δt is just the FWHM. Variations of T_{av} and Δt with x , as derived from Fig. 10 (c), are shown in Fig. 11 (a). Then the Arrhenius equation $D = D_0 \exp(-E_a/k_B T_{av})$ for diffusion coefficient D can be used to calculate the square L^2 of the diffusion length as $L^2 \propto D\Delta t$, which itself should be proportional to σ^2 measured experimentally, if the TSM is valid. Here, D_0 is a pre-exponential factor, E_a is the activation energy for diffusion, and k_B is the Boltzmann's constant. According to the literature,⁴⁷ D_0 and E_a for Pd diffusion in Si are 3.13×10^{-4} cm²/s and 1.1 eV, respectively. For Ni diffusion in Si, these values are 6×10^{-4} cm²/s and 0.67 eV, respectively.

Plots of the diffusion coefficients thus calculated are shown in Fig. 11 (b). It can readily be inferred from the figure that although the two diffusion coefficients follow the same x variation, they are three orders of magnitude apart. Figure 7, however, suggest that if the experimentally observed change in interfacial width on irradiation is due to interdiffusion, both the diffusion coefficients, or at least the effective diffusion coefficients, must be almost equal. So, the experimental observations can not be a result of simple solid state diffusion. Liquid (molten) state diffusion has already been ruled out. In this scenario, only one proposition seems to work: SHI irradiation must have produced an enormous amount of defects, thereby reducing the activation energy for diffusion to such an extent that the effective diffusion coefficients are liquid-like. The liquid state diffusivities are of the same order of magnitude (10^{-5} cm²/s).^{8,48,49} Once the activation energy is reduced, even the Ar⁺ ion sputtering must be able to produce the observed diffusion. So, we ignore the magnitudes of the diffusion coefficients and focus only on their variation with x . We can see, from Fig. 11 (b), that this variation is monotonic, and certainly does not follow a concave upward trend. This can be considered as the second milestone for comparison, where experimental results do not seem to be reproduced by theory. Next, since Δt changes only by a factor of two from Pd to Ni, L^2 must also follow the same trend. The variation of L^2 with x determined this way has been plotted in Fig. 11 (c) for interdiffusion of both Pd and Ni in Si. As can be seen, this no way resembles a concave upward curve with a minimum. The last thing to check is the influence of x -dependence of crystallite size, based on the reports,^{50,51} on nanometric size effects on irradiation induced changes. The crystallite sizes of all the samples as determined using the Debye-Scherrer equation⁵² applied to the XRD patterns (Fig. 1) range from 20 nm to 60 nm. This size variation hardly changes the influence of SHI's, as can be seen in the references 50 - 51. So, at last, it seems that the TSM, which has so far been successful in explaining the experimental outcomes of SHI - matter interaction, is not able to explain the experimental results of SHI mixing presented in this work. Perhaps some other considerations, apart from the TSM suggested molten state

diffusion for SHI mixing, need to be explored.

IV. CONCLUSION

The thermal spike model of SHI - matter interaction has been assessed via its applicability in SHI mixing by comparing the results of (i) 100 MeV Au ion irradiation of Pd_{1-x}Ni_x thin films deposited on Si, and (ii) calculations based on density functional theory and the model. The key concept behind the calculations is the well accepted notion that SHI mixing is a result of diffusion in transient molten state created by the SHI. Although no mixing has been detected in RBS spectra, a considerable amount is observable on Ar⁺ ion sputtering based depth profiling associated with XPS characterizations. This is proposed to be possible due to both the high spatial resolution obtainable from XPS and the sputtering assisted mixing. Since the latter has to be uniform in all the samples, its role can be ignored in the study of x dependence of mixing, which has been the prime focus of the work. The irradiation induced change in the variance of the depth profile determined from the XPS spectra follows an x variation which is concave upward with a pronounced minimum. DFT has been used to derive the x dependences of electronic specific heat and electron-phonon coupling strength. These data have been used as an input to the TTM equations appropriate to the thermal spike model to calculate the evolution of lattice temperature with time at various radial distances from the ion path. Finally, a quantity L^2 proportional to the variance is calculated, and its variation with x is derived. If the TSM, along with the conception that mixing is a result of molten state diffusion is valid, L^2 must also vary with x along a curve which is concave upward with minimum. However, L^2 increases monotonically with x without any minimum, and thus is not in accordance with the experimental observations. Even the crystallite size variation, as determined from the XRD patterns, can not account for the observed x -variation of σ^2 . This leads to the conjecture that the combination of the TSM and the molten state diffusion is probably an insufficient description of SHI mixing, and hence the underlying mechanism requires further considerations.

V. ACKNOWLEDGEMENTS

D. Kabiraj and S. R. Abhilash of the Target Lab of IUAC, New Delhi are acknowledged for their help in sample preparation. The help provided by S. Ojha and G. R. Umopathy of PARAS facility of IUAC, New Delhi in RBS measurements is also acknowledged. The authors

also acknowledge the support by the Pelletron Accelerator Group of IUAC, New Delhi for irradiations. Many useful discussions with M. Toulemonde are also highly acknowledged. Paramita Patra is thankful to Indian In-

stitute of Technology Kharagpur for the financial support to carry out the research work.

* patro.paro@phy.iitkgp.ernet.in

† sanjeev@phy.iitkgp.ernet.in

¹ L. C. Northcliffe, *Ann. Rev. Nucl. Sci.* **13**, 67 (1963).

² B. Schattat, W. Bolse, S. Klaumünzer, F. Harbsmeier and A. Jasenek, *Appl. Phys. A* **76**, 165 (2003).

³ C. L. Tracy, M. Lang, F. Zhang, C. Trautmann and R. C. Ewing, *Phys. Rev. B* **92**, 174101 (2015).

⁴ S. K. Srivastava, S. A. Khan, P. Sudheer Babu and D. K. Avasthi, *Nucl. Instrum. Methods B* **332**, 377 (2014).

⁵ Z. G. Wang, C. Dufour, E. Paumier and M. Toulemonde, *J. Phys.: Condensed Matter* **6**, 6733 (1994).

⁶ M. Toulemonde, W. Assmann, C. Trautmann and F. Grüner, *Phys. Rev. Lett.* **88**, 057602 (2002).

⁷ A. Gupta and D. K. Avasthi, *Phys. Rev. B* **64**, 155407 (2001).

⁸ S. K. Srivastava, D. K. Avasthi, W. Assmann, Z. G. Wang, H. Kucal, E. Jacquet, H. D. Carstanjen and M. Toulemonde, *Phys. Rev. B* **71**, 193405 (2005).

⁹ C. Dufour, A. Audouard, F. Beuneu, J. Dural, J. P. Girard, A. Hairie, M. Levalois, E. Paumier and M. Toulemonde, *J. Phys.: Condensed Matter* **5**, 4573 (1993).

¹⁰ M. Toulemonde, J. M. Costantini, Ch. Dufour, A. Meftah, E. Paumier and F. Studer, *Nucl. Instrum. Methods B* **116**, 37 (1996).

¹¹ B. R. Chakraborty, D. Kabiraj, K. Diva, J. C. Pivin and D. K. Avasthi, *Nucl. Instrum. Methods B* **244**, 209 (2006).

¹² K. Diva, D. Kabiraj, B. R. Chakraborty, S. M. Shivaprasad and D. K. Avasthi, *Nucl. Instrum. Methods B* **222**, 169 (2004).

¹³ Z. Lin, L. V Zhigilei and V. Celli, *Phys. Rev. B* **77**, 075133 (2008).

¹⁴ D. A. Papaconstantopoulos, L. L. Boyer, B. M. Klein, A. R. Williams, V. L. Moruzzi and J. F. Janak, *Phys. Rev. B* **15**, 4221 (1977).

¹⁵ G. Grimvall, *Phys. Scripta* **14**, 63 (1976).

¹⁶ A. K. Giri and G. B. Mitra, *Physica B* **138**, 41 (1986).

¹⁷ P. Patra and S. K. Srivastava, *Nucl. Instrum. Methods B* **379**, 9 (2016).

¹⁸ C. G. Schön and G. Inden, *Acta Materialia* **46**, 4219 (1998).

¹⁹ P. Franke and D. Neuschütz, Scientific Group ThermoData Europe (SGTE) Ni-Pd. In: Binary Systems. Part 4: Binary Systems from Mn-Mo to Y-Zr. Landolt-Börnstein - Group IV Physical Chemistry, Franke P., Neuschütz D. (eds.) (Springer, Berlin, Heidelberg), vol 19B4.

²⁰ B. Y. Tsaur, Z. L. Liao and J. W. Mayer, *Appl. Phys. Lett.* **34**, 2 (1979).

²¹ J. Desimoni, A. Traverse and M. G. Medici, *Nucl. Instrum. Methods B* **72**, 197 (1992).

²² J. F. Zeigler, J. P. Biersack and U. Littmark, *The Stopping and Ranges of Ions in Solids* (Pergamon, New York, 1985) Vol.1.

²³ P. Blaha, K. Schwarz, G. Madsen, D. Kvasnicka and J. Luitz, *Wien2K an Augmented Plane Wave + Local Orbitals Programme for Calculating Crystal Properties* Karlheinz Schwarz (Techn. Universität Wien, Austria, 1999).

²⁴ F. Birch, *Phys. Rev.* **71**, 809 (1947).

²⁵ F. D. Murnaghan, *Finite Deformation of an Elastic Solid* (Wiley, New York, 1951).

²⁶ J. P. Perdew, K. Burke and M. Ernzerhof, *Phys. Rev. Lett.* **77**, 3865 (1996).

²⁷ S. Cottenier, *Density Functional Theory and the Family of (L)APW-methods: A Step-By-Step Introduction* (K. U. Leuven, Belgium: Instituutvoor Kern-en Stralingsfysica, 2002).

²⁸ A. Chettah, H. Kucal, Z. G. Wang, M. Kac, A. Meftah and M. Toulemonde, *Nucl. Instrum. Methods B* **267** 2719 (2009).

²⁹ http://www.ccp14.ac.uk/ccp/web-mirrors/powdcell/a_v/v_1/powder/

³⁰ A. Dahal, J. Gunasekera, L. Harringer, D. K. Singh and D. J. Singh, *J. Alloys. Comp.* **672**, 110 (2016).

³¹ https://materials.springer.com/isp/crystallographic/docs/sd_0261223

³² https://materials.springer.com/isp/crystallographic/docs/sd_0526418

³³ N. Wälchli, E. Kampshoff, A. Menck and K. Kern, *Surf. Sci.* **382** 705 (1997).

³⁴ L. Thomé, T. Benkoulal, J. Jagielski and B. Vassent, *Europhys. Lett.* **20** (5) 413 (1992).

³⁵ <https://home.mpcdf.mpg.de/mam/Version7.html>

³⁶ S. Hofmann, *Rep. Prog. Phys.* **61**, 827 (1998).

³⁷ V. Kumar, D. Tománek and K. H. Bennemann, *Solid State Commun.* **39**, 987 (1981).

³⁸ A. Kumar, T. Shripathi and P. C. Srivastava, *J. Sci.: Adv. Mater. Dev.* **1**, 290 (2016).

³⁹ <https://srdata.nist.gov/xps/ElmSpectralSrch.aspx?selEnergy=PE>

⁴⁰ Y. Takagi, C-H. Hwang, H. Sekizawa and K. Kawamura, *Jpn. J. Appl. Phys.* **24**, 390 (1985).

⁴¹ Q. Wei, Y-S. Shi, K-Q. Sun and B-Q. Xu, *Chem. Commun.* **52**, 3026 (2016).

⁴² Y. Cao, L. Nyborg and U. Jelvestam, *Surf. Interf. Anal.* **41**, 471 (2009).

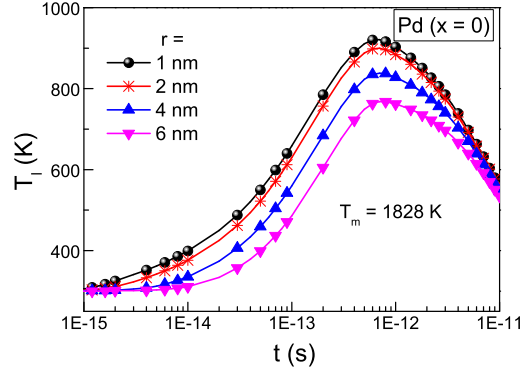
⁴³ X. Chen, J. Guan, G. Sha, Z. Gao, C. T. Williams and C. Liang, *RSC Adv.* **4**, 653 (2014).

⁴⁴ H. Gabasch, W. Unterberger, K. Hayek, B. Klötzer, E. Kleimenov, D. Teschner, S. Zafeiratos, M. Hävecker, A. Knop-Gericke, R. Schlögl, J. Han, F. H. Ribeiro, B. Aszaloss-Kiss, T. Curtin and D. Zemlyanov, *Surf. Sci.* **600**, 2980 (2006).

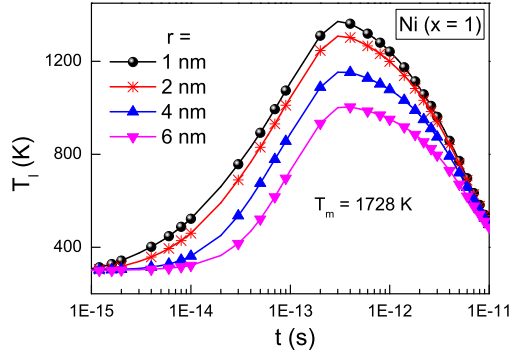
⁴⁵ M. Müller and G. Münster, [arXiv:cond-mat/0405673v3](https://arxiv.org/abs/cond-mat/0405673v3) [cond-mat.stat-mech].

⁴⁶ P. Swain, S. K. Srivastava and S. K. Srivastava, *Solid State Commun.* **260**, 10 (2017).

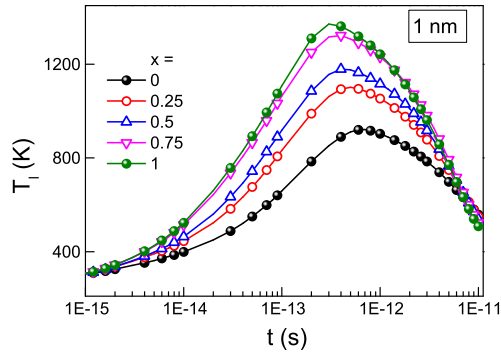
- ⁴⁷ http://pearson.mse.ufl.edu/semic_properties/data/5029.pdf
- ⁴⁸ X. Liu, in Diffusion in Liquids, Masters Thesis, TU Delft (2012).
- ⁴⁹ A. A. Pradhan and J. Heideger, *Can. J. Chem. Engg.* **49**, 10 (1971).
- ⁵⁰ A. Bertholet, S. Hémon, F. Gourbilleau, C. Dufour, E. Dooryhée and E. Paumier, *Nucl. Instrum. Methods B* **146**, 437 (1998).
- ⁵¹ A. Bertholet, S. Hémon, F. Gourbilleau, C. Dufour, B. Domengès and E. Paumier, *Phil. Mag. A* **80**, 2257 (2000).
- ⁵² A. L. Patterson, *Phys. Rev.* **56**, 978 (1939).



(a)



(b)



(c)

FIG. 10: Evolution of lattice temperature with time for (a) $x = 0$ and (b) $x = 1$, with radial distance from ion path as a parameter, and (c) at 1 nm radial distance for all compositions. Melting temperature T_m ¹⁹ is indicated.

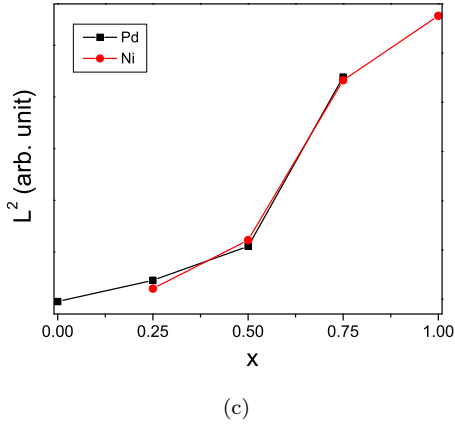
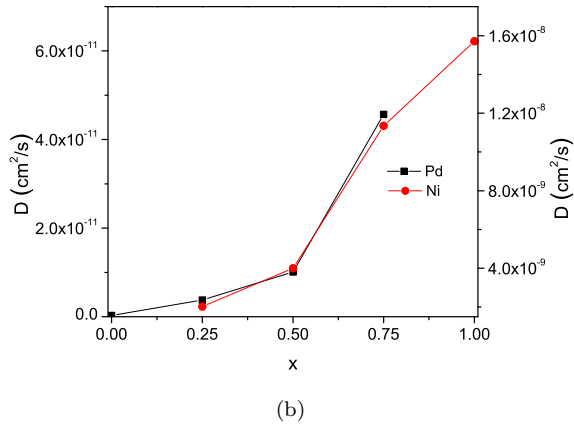
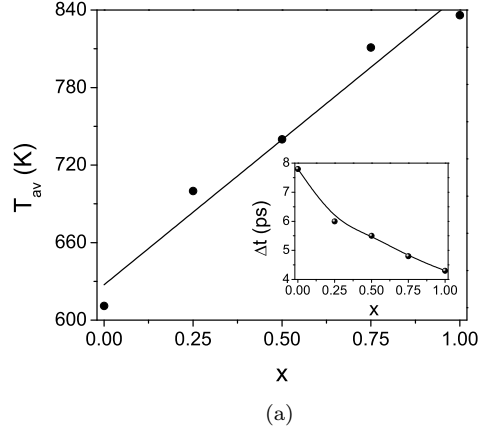


FIG. 11: (a) Variations of average lattice temperature T_{av} at 1 nm radial distance from ion path, and of the duration Δt (inset) of this temperature with x . (b) Pd and Ni diffusion coefficients at these temperatures as a function of x . (c) L^2 versus x curves for Pd and Ni. Lines are a guide to the eyes.